https://doi.org/10.5194/gmd-2019-173
Preprint. Discussion started: 23 July 2019

Geoscientific Model Development
Discussions

Short-term forecasting of regional biospheric CO_2 fluxes in Europe using a light-use-efficiency model

Jinxuan Chen[1], Christoph Gerbig[1], Julia Marshall[1], and Kai Uwe Totsche[2]

[1]Department Biogeochemical Systems, Max Plank Institute for Biogeochemistry, Jena, 07745, Germany
[2]Friedrich Schiller University, Jena, 07743, Germany

Correspondence to: Jinxuan Chen (jichen@bgc-jena.mpg.de)

Abstract. Forecasting atmospheric CO_2 concentrations on synoptic time scales (~days) can benefit the planning of field campaigns by better predicting the location of important gradients. One aspect of this, accurately predicting the day-to-day variation in biospheric fluxes poses a major challenge. This research aims to investigate the feasibility of using a diagnostic light-use-efficiency model, the Vegetation Photosynthesis Respiration Model (VPRM), to forecast biospheric CO_2 fluxes on the time scale of a few days. As input the VPRM model requires downward shortwave radiation, 2 m temperature, and Enhanced Vegetation Index (EVI) and Land Surface Water Index (LSWI), both of which are calculated from MODIS reflectance measurements. Flux forecasts were performed by extrapolating the model input into the future, i.e. using downward shortwave radiation and temperature from a numerical weather prediction (NWP) model, as well as extrapolating the MODIS indices to calculate future biospheric CO_2 fluxes with VPRM. A hindcast for biospheric CO_2 fluxes in Europe in 2014 has been done and compared to eddy covariance flux measurements to assess the uncertainty from different aspects of the forecasting system. In total the range-normalized mean absolute error (normalized) of the 5 day flux forecast at daily timescales is 7.1%, while the error for the model itself is 15.9%. The largest forecast error source comes from the meteorological data, which fail to accurately predict cloud cover, leading to overestimated shortwave radiation in the model. The error contribution from all error sources is similar at each flux observation site, and is not significantly dependent on vegetation type.

1 Introduction

Human activities have significantly influenced the carbon cycle of the earth system since industrialization, with the accumulation of greenhouse gases in the atmosphere leading to radiative forcing and climate change (IPCC, 2014). The carbon exchange between the surface and the atmospheric still remains largely uncertain due to the complexity of processes and a lack of observations (Le Quere et al., 2009). Therefore more measurements are needed, especially over emission hotspots and regions lacking observations. Field campaigns to measure greenhouse gases, such as research flights and measurements in remote areas, can fill the observation gap in the troposphere and over regions not covered by existing networks, but they are often time-limited. To make the best use of these limited measurements, field campaigns require careful planning. An

https://doi.org/10.5194/gmd-2019-173
Preprint. Discussion started: 23 July 2019

atmospheric CO_2 forecast on synoptic time scales (~days) can be helpful in such cases, for it provides an estimate of what signals are expected during the experiment and a physical explanation of the observations.

The research campaign CoMet (Carbon dioxide and Methane Mission), organized by the Deutsches Zentrum für Luft- und Raumfahrt (DLR), made a series of airborne and ground-based measurements of greenhouse gases in Europe. The campaign took place from May 15th to June 12th 2018, during which three aircraft participated, including the High Altitude and LOng Range Research Aircraft (HALO) and three light aircraft. During the campaign the HALO was equipped with an Integrated Path Differential Absorption (IPDA) Lidar (CHARM-F) (Amediek et al., 2017), and carried out nine flights with a total of 65 flight hours. Continuous online in situ CO_2, CO, CH_4 and water vapor measurements were also made onboard with the Jena Instrument for Greenhouse gas measurements (JIG) and air samples were collected with the Jena Air Sampler (JAS). The campaign performed measurements over different surfaces from northern Europe to North Africa to assess and validate the new remote sensing instrument CHARM-F. Special attention was paid to two areas: Berlin (and nearby power plants) and the Upper Silesian basin, which are significant European point sources of CO_2 and CH_4 respectively. Ground-based and light aircraft measurements were also made in the two regions with the remote sensing instrument Methane Airborne Mapper (MAMAP) (Gerilowski et al., 2011) and portable ground-based Fourier Transform Infrared Spectrometers (FTIR) (Butz et al., 2017).

During the planning of the campaign, a CO_2 and CH_4 forecasting system was developed to support the mission; this paper focuses on the biogenic fluxes for the CO_2 component. The forecast provided 5 day CO_2 forecast fields at a fine spatial resolution (2 km x 2 km) within the observing area, and a coarser resolution over the European domain (10 km x 10 km). The forecast product is not only helpful in terms of planning observations, offering meteorology and GHG fields to capture CO_2/CH_4 plumes, but can also provide a priori vertical information for the retrieval of remote sensing observations.

There are several existing models that can simulate atmospheric CO_2 on an appropriate scale, including Eulerian mesoscale models such as WRF-GHG (Beck et al., 2011;Pillai et al., 2016) and CHIMERE (Aulagnier et al., 2010). These models consist of an atmospheric tracer transport model coupled to fluxes representing the source and sink processes of CO_2. By providing meteorological forecast fields and future fluxes of CO_2 to the model, the forecast CO_2 concentration fields can be obtained. The challenge of CO_2 forecasting comes with the provision of accurate CO_2 flux variations on sub-daily time scales. A global atmospheric CO_2 forecast system has been developed as part of the Monitoring of Atmospheric Composition and Climate – Interim Implementation (MACC-II) service (Agusti-Panareda et al., 2014;Agusti-Panareda et al., 2016). These studies have shown that although transport plays a first order role in synoptic CO_2 variability, the day-to-day variability of NEE also plays an important role. Therefore it is crucial for CO_2 forecasts to capture the day-to-day NEE variability in real-time, instead of using climatological values.

There are many models that can simulate biospheric CO_2 NEE on hourly time scales (Boussetta et al., 2013;Mahadevan et al., 2008). These models can be briefly grouped into two types: process-based models and light use efficiency (LUE) models. Process-based models use meteorological data as input and simulate the physiological processes of vegetation, for example BIOME-BGC (Running and Hunt

https://doi.org/10.5194/gmd-2019-173
Preprint. Discussion started: 23 July 2019

Geoscientific Model Development Discussions Open Access EGU

Jr, 1993), TEM (Zhuang et al., 2003) or the Carbon Exchange in the Vegetation-Soil-Atmosphere model (CEVSA) (Woodward et al., 1995). Such models usually need a number of parameters to describe the complex vegetation processes responding to meteorological drivers. The second type, LUE models, regard ecosystem gross primary production (GPP) as the product of photosynthetically active radiation (PAR), the fraction of photosynthetically active radiation absorbed by the photosynthetically active portion of the vegetation ($FAPAR_{PAV}$), and the radiation use efficiency (ε). Such models include the Vegetation Photosynthesis and Respiration Model (VPRM) (Xiao et al., 2004;Mahadevan et al., 2008), the MODIS Daily Photosynthesis Model (Running et al., 2000) and the Carnegie-Ames-Stanford Approach (CASA) (Potter et al., 1993).

The CO_2 forecast in MACC-II uses the process-based model CTESSEL to compute biospheric CO_2 fluxes and evapotranspiration online (Boussetta et al., 2013;Agusti-Panareda et al., 2016), which makes the two variables consistent in the forecast system. However the challenge of providing accurate CO_2 fluxes is due to the complexity of vegetation processes and the lack of near-real-time (NRT) observations on vegetation state. Therefore, using a LUE model for CO_2 flux forecasting, which is a data-driven approach having less parameters compared to process-based models, is a possible way to improve the quality of CO_2 fluxes in forecasting. It should be note that unlike the Copernicus Atmosphere Monitoring Service (CAMS) CO_2 forecasting which is operational and global, we target to build a regional CO_2 forecast system and only operate the forecast within a shorter period (e.g. several months). Therefore the issue of CO_2 budget conservation is less important comparing to a operational global forecast model. In our case, we predict CO_2 fluxes based on the LUE model VPRM, which is driven by the Enhanced Vegetation Index (EVI) and the Land Surface Water Index (LSWI) as well as the meteorological variables 2 m air temperature and downward shortwave radiation. The EVI and LSWI are derived from Moderate Resolution Imaging Spectroradiometer (MODIS) reflectance data, in which the MOD09A1N product provides NRT surface reflectance data, thus the NRT observations on vegetation state can be used in flux forecasting. VPRM has a strong predictive ability for NEE while maintaining simplicity in having only four parameters for each of the seven vegetation types, which makes it suitable for our case. The flux forecast is then made by predicting the input of VPRM, for which different prediction methods were tested. Although the uncertainties in VPRM have been well assessed by previous research(Lin et al., 2011), it is still unknown how does such LUE model perform regarding of flux forecasting in synoptic time scale.

This study describes the development and assessment of a biospheric CO_2 flux forecast based on the LUE model VPRM, with the goal of providing accurate hourly 5 day flux forecasts. By using a hindcast and comparing to flux tower sites across Europe the error in the prediction is evaluated, and the predictive ability of the CO_2 flux forecasts is assessed.

2 Methodology

The CO_2 flux forecast consists of two steps as shown in Figure 1. Model inputs are first predicted 5 days into the future, then NEE is estimated based on the standard VPRM model, using parameters optimized in previous studies (Kountouris et al., 2018). Each input which must be forecast results in

https://doi.org/10.5194/gmd-2019-173
Preprint. Discussion started: 23 July 2019

corresponding errors. We systematically evaluate the flux forecasting error associated with each of these predictands.

This section describes the framework of the VPRM forecasting model for biospheric CO_2 fluxes, as well as the method used to evaluate the error introduced by each element of the forecast.

For the meteorological input data, we use hourly ECMWF 5 day forecasts of temperature and short wave radiation. The EVI and LSWI indices are derived from MODIS surface reflectance data. These provide the indices for an average of the past eight days, and we forecast these indices for the next five days based on linear extrapolation or persistence. We then use these predicted input data to generate NEE using VPRM.

2.1 VPRM data processing

2.1.1 Standard processing for past periods

The flux estimation is based on VPRM, a light use efficiency (LUE) model that calculates GPP with remote sensing data and meteorological data as inputs. The equation of GPP estimation is as follow:

$$GPP = \varepsilon \times FAPAR_{PAV} \times \frac{1}{1+PAR/PAR_0} \times PAR \quad (1)$$

The light use efficiency ε can be decomposed as:

$$\varepsilon = \lambda \times T_{scalar} \times W_{scalar} \times P_{scalar} \quad (2)$$

Where T_{scalar}, W_{scalar} and P_{scalar} represent the temperature sensitivity of photosynthesis, the water stress effect, and the effects of leaf age on canopy photosynthesis, respectively, while λ is an adjustable parameter in the model. Among them, T_{scalar} is estimated from air temperature, and W_{scalar} and P_{scalar} are estimated from LSWI. See details in Mahadevan et al. 2008.

The $FAPAR_{PAV}$ in the model is estimated as a linear function of EVI, and PAR is closely correlated with downward shortwave radiation. Therefore the complete expression for GPP in VPRM is:

$$GPP = (\lambda \times T_{scalar} \times W_{scalar} \times P_{scalar}) \times EVI \times \frac{1}{1+\frac{PAR}{PAR_0}} \times PAR \quad (3)$$

While the vegetation respiration is estimated by a simple linear model:

$$R = \alpha \times T_{air} + \beta \quad (4)$$

Where T_{air} is the air temperature and α and β are vegetation-class-specific parameters.

The input of VPRM can be categorized into two groups: remote sensing data and meteorological data. The remote sensing data consist of EVI and LSWI at 10 km spatial resolution (same resolution with atmospheric transport model), where the EVI and LSWI are aggregated from MODIS surface reflectance 8 day L3 Global 500m (MOD09A1) version 6 data. It should be noted that in the forecasting model, the MODIS NRT surface reflectance data (MOD09A1N) would be used. A locally weighted least squares (LOESS) filter (α=0.17) is then applied to reduce the noise. The vegetation classification map (SYNMAP) (Jung et al., 2006) is also a product derived from remote sensing. The meteorological data include air temperature at 2m and downward shortwave radiation at the surface, which are obtained from a numerical weather prediction (NWP) model product, in our case the operational forecast archive from the European Centre for Medium-Range Weather Forecasts (ECMWF). In VPRM, there are four parameters (λ, PAR_0, α, β) for each vegetation type. Model calibration for these parameters has been done using flux measurements in Europe in 2007(Kountouris et al., 2018).

2.1.2 Processing for flux prediction

To use this diagnostic model in a predictive mode, we need to forecast all VPRM input variables five days into the future. Remote sensing data and meteorological data are predicted in different ways.

For the meteorological data, forecasts from a numerical weather prediction (NWP) model are needed. In this study, in order to assess the errors brought in by the meteorological forecasting, 5 day forecasts of 2 m temperature and downward shortwave radiation at the surface for each day of the year were used. The meteorological forecast is from the ECMWF operational forecast archive, with class "od" and type "fc".

As for the remote sensing data, three sources of error had to be considered: the error induced by using the NRT version of the MODIS reflectances rather than the final product, the error of estimating the value of the indices into the future, and the effect of the LOESS filter on the end value of the dataset.

We begin by describing the LOESS filter. This filter is usually applied to a full year of data, and when smoothing a truncated dataset there is an edge effect, meaning that when new data are added to the time series the smoothing is repeated, the output at the former edge point will change slightly. In the following section we define the error caused by such an edge effect as "error due to data truncation".

Following the filtering, the smoothed data are extrapolated five days into the future, either by linear extrapolation or by assuming persistence. The optimal extrapolation method was selected after testing the error contribution of each method.

The last error source comes from the difference between MODIS NRT and the standard product. The standard product is processed with the best available ancillary, calibration, and geolocation information while changes have been made in the NRT processing to expedite the data availability (See https://earthdata.nasa.gov/earth-observation-data/near-real-time/near-real-time-versus-standard-products).

2.2 Uncertainty analysis

The potential error sources of this flux forecasting system are as follows: (1) the VPRM model itself, (2) using analysis rather than site-level meteorological data, (3) using ECMWF forecast meteorology, (4) using NRT MODIS data, (5) using LOESS filtering to smooth the MODIS data, and (6) the prediction of MODIS data. The error (6) contains two parts: (6a) EVI prediction and (6b) LSWI prediction. In the following discussion we use the numbering (1) to (6) to denote these error sources. We define (1) as the "model error", and (2) to (6) as the "forecast errors". The model error has been well described in previous research, and in general VPRM shows a good predictive ability (Mahadevan et al., 2008). In this study, we aim to quantify the forecast error, and the error contribution from each of the error sources.

In order to evaluate both the model error and the forecast error, a hindcast using the CO_2 flux forecast model has been done for the year 2014 for Europe. The evaluation and comparison was done at two spatial levels: at the flux observation site level, and at the European domain level (1/8° longitude ×

https://doi.org/10.5194/gmd-2019-173
Preprint. Discussion started: 23 July 2019

1/12° latitude). The comparison at site level aims to evaluate both the model error and the forecast error at locations with different vegetation types, while over the European domain, the aim is to investigate the spatial pattern of each forecast error term.

The surface CO_2 flux observation data comes from eddy covariance tower measurements from the FLUXNET2015 tier one (open data) dataset (Baldocchi et al., 2001). Thirty-three European observation sites for which both MODIS data and flux measurements for 2014 are available were selected for data-model comparison. The selected sites' ID, location, vegetation type and their data DOI are listed in table 1.

To test the error contribution of the model and the 5 day flux forecast, the following experiments using the VPRM forecast model were carried out to evaluate the error contribution from different sources separately. Although the CO_2 flux forecast targets hourly flux prediction for the next 5 days, model error and forecast error were analyzed on a daily time scale, as this scale is more relevant for synoptic CO_2 variability in the atmosphere.

The control simulation uses standard VPRM as a reference model with "perfect" input, meaning the MODIS EVI and LSWI standard products as well as shortwave radiation and temperature observed at the flux site. By comparing the modeled NEE to flux measurements, we can estimate the VPRM model error (1).

The experimental simulations a to f then included the error sources (2) to (6) in the VPRM model input data separately, and these are compared to the reference simulation in order to isolate these individual error contributions. The experiments aim to estimate the upper limit of forecast error, therefore in simulations b and f, 96 h to 120 h meteorological forecasts, i.e. the last day (5th) of a 5 day forecast, were used for each day of the year. For simulations d and f, since the MODIS EVI and LSWI products has an 8 day period, MODIS data were first linearly interpolated to a daily scale. Then for each day of the year MODIS data on the n^{th} day were predicted from data on the n-5^{th} day.

There is a challenge in simulation e in that there are no achieved NRT data for 2014, thus it is impossible to have a comparison on the same basis with other the simulations. Instead we look into the model's sensitivity of NEE to EVI and LSWI bias, and also compare the NRT EVI and LSWI, which we archived from February to June in 2018 for 120 days, to the standard MODIS product over the save period. In this way we were able to estimate the magnitude of the NRT indices' error and its impact on the model's output NEE.

In order to make the 33 different site results comparable, the simulation output NEE was first aggregated to daily averages, and then normalized by the range (i.e. the difference between maximum and minimum) of annual NEE at each site. The $bias_{NEE}$, which is defined as the output NEE from the experimental simulation minus the same variable from the reference model, was then calculated and normalized by the same scalar at each site. By applying such a normalization, positive and negative NEE keep their sign, and the normalized $bias_{NEE}$ represents a fractional bias compared to the range of annual variation. (For example a normalized $bias_{NEE}$ of 0.1 means that the magnitude of the bias equals 10% of the annual variation.) The mean of the absolute $bias_{NEE}$ will be the mean absolute error (MAE), which is also used as a measure for error in this research. An example of such normalization is shown for the station BE-Bra in Figure 2.

https://doi.org/10.5194/gmd-2019-173
Preprint. Discussion started: 23 July 2019

Geoscientific Model Development
Discussions

3 Results and Discussion

3.1 Error attribution on site level

By comparing the NEE output from each experimental simulation, the impact of each error source on flux forecasting can be isolated and evaluated. The normalized mean absolute error (MAE) of NEE at all 33 sites is presented in Table 3. The MAE of the total forecast error is 0.071, which is smaller than the VPRM model error of 0.159. This indicates that the forecast model is reasonably capable of predicting fluxes on diurnal time scales.

3.1.1 Meteorological error

Among all forecast errors, the meteorological error accounts for the largest contribution. The meteorological error can be decomposed into (2) analysis error and (3) meteorological forecast error. The former corresponds to using meteorological analysis rather than observational data, while the latter comes from the numerical meteorological forecasting, and can be estimated by comparing simulations b and a. The analysis error and meteorological forecast error are of the same order of magnitude, namely 0.046 and 0.065 respectively.

The meteorological error is then analyzed further by dividing it into the photosynthetic part ($bias_{-GPP}$) and the non-photosynthetic respiration part ($bias_R$). The bias (defined in 2.2) distributions of 33×365 data points are shown in Figure 3.

In figure 3, panels (a), (b) and (c) share the same x-axis, and the bias in the y-axes can be combined as $bias_{NEE} = bias_{-GPP} + bias_{R.}$ Because a positive GPP bias will lead to a negative NEE bias, -GPP is used here to show its contribution to NEE. $Bias_{-GPP}$ has a larger vertical spread towards negative values, which means a systematic bias in GPP. In contrast $bias_R$ is basically symmetric about zero, which implies that the errors in temperature are random.

This indicates that $bias_{NEE}$ is dominated by the photosynthetic part $bias_{-GPP}$. Knowing that $bias_{NEE}$ is the result of biases in two meteorological variables used in the simulation, air temperature and downward shortwave radiation (SW), we can conclude that it is the errors in shortwave radiation that mainly contribute to the meteorological error. From the bias distribution in figure 3(b) we can also see that the GPP bias is concentrated in negative values, meaning a stronger CO_2 uptake than the reference case.

This pattern can also be seen at site level, as shown in figure 4 for the station BE-Bra. Figure 4(a) shows that during summer, there are several episodes when the forecast fails to correctly predict the low SW (indicating more cloud cover) in the observations. In figure 4(b) negative $bias_{-GPP}$ and $bias_{NEE}$ signals match well with these episode. It confirms the conclusion that the meteorological error is dominated by errors in SW, and it is due to incorrect prediction of clouds during summer.

3.1.2 MODIS error

The MODIS error consists of three parts: using NRT products, using extrapolation of indices, and using truncated time series, which are represented in simulations c, d and e respectively. In general, the MODIS error is less important compared to the meteorological error, and the errors due to data truncation, EVI extrapolation and LSWI extrapolation result in errors on the same order of magnitude:

https://doi.org/10.5194/gmd-2019-173
Preprint. Discussion started: 23 July 2019

Geoscientific Model Development Discussions
Open Access
EGU

0.015, 0.013 and 0.010 respectively.

As described in section 2.1.1, the MODIS input data first need to be smoothed by a LOESS filter to reduce the noise. LOESS performs a local regression on the time series. Because the point at the end of the time series lacks a constraint from future data, it results in an error when the data are truncated. This error source is evaluated in simulation c, where for each 8 day value, only data before this time are filtered. Thus the only difference between simulation c and the reference simulation is whether each MODIS-derived index is constrained by all local data or only constrained by preceding data. Comparing simulation c and the reference simulation finds that the error due to lack of constraint from future MODIS data introduces an MAE of 0.015.

For MODIS data extrapolation, different methods were tested in an attempt to minimize forecast error. Climatological values of EVI and LSWI were considered, but they lack the advantage of a data-driven approach for realistic estimation. After testing various alternatives, two simple methods were considered: linear extrapolation based on the last three data points and persistence (assuming the indices stay the same for the next 5 days). Figure 5 shows the NEE bias distribution by using linear extrapolation or persistence to predict EVI and LSWI. For both indices, using the assumption of persistence results in a smaller error. The biases for the two extrapolation methods have similar distributions, but there are more outliers for linear extrapolation. This is due to the fact that linear extrapolation results in larger errors when the data are fluctuating.

Finally, the difference between using MODIS NRT data and standard data has to be considered. This includes the effect of using different attitude and ephemeris data in processing, as well as using different ancillary data products for the Level 2 processing. For L2 Land Surface Reflectance data, National Oceanic and Atmospheric Administration Global Forecast System (GFS) ancillary product are used instead of Global Data Assimilation System (GDAS) used in the standard processing (This is described at NASA's Land, Atmosphere Near real-time Capability for EOS (LANCE) website https://earthdata.nasa.gov/earth-observation-data/near-real-time/near-real-time-versus-standard-products).

This presented a challenge, as no MODIS NRT data were archived for the test year 2014. Thus it was impossible to carry out a similar error evaluation as was done for other error sources. Therefore we first use NRT EVI and LSWI that we archived for 120 days from February to June 2018 to calculate the MAE of the two indices to standard products at all flux sites. The MAE of NRT EVI and LSWI for all sites are 0.018 and 0.026 respectively. Considering the mean EVI and LSWI, which are 0.21 and 0.11 during this period, the magnitude of NRT EVI error is less than 10% of EVI's magnitude while the number is 24% for the magnitude of NRT LSWI error.

The impact of these NRT indices errors on the model is determined by the model's sensitivity to EVI and LSWI. To investigate this sensitivity, we use the result from simulation d and the reference simulation, and look into the difference in input EVI and LSWI, and the corresponding difference in output NEE. The model's sensitivity is different during the growing and the non-growing seasons, as in the non-growing season there would be no vegetation production anyway from a slight change of EVI and LSWI.

https://doi.org/10.5194/gmd-2019-173
Preprint. Discussion started: 23 July 2019

Geoscientific Model Development Discussions

Therefore the model sensitivity is analyzed for each season separately, as shown in table 4. Difference in indices and the corresponding difference in daily NEE are applied with linear regression, and the rate of the linear function is regarded as model sensitivity. The maximum sensitivity for both EVI and LSWI both is in summer, with -9.11 [μmole m^{-2} s^{-1} EVI^{-1}] and -6.29 [μmole m^{-2} s^{-1} $LSWI^{-1}$] respectively. By assuming that the 120 days of archived NRT data is representative for MODIS NRT error, we can estimate the upper limit of forecasting error (4), as it is shown in Figure 6. The normalized NEE error in figure 6 is calculated by using MODIS NRT error times the model sensitivity, and then normalized by the same scalar in previous analysis at each site. Therefore the error here is comparable to the MAE in table 3 if we assume the MODIS NRT data in the year 2014 and 2018 have similar error structure. The NEE error for all sites due to NRT-EVI and NRT-LSWI are 0.024 and 0.025 respectively, which is still less important comparing to the meteorology error in table 3.

3.1.3 VPRM model error

Unlike the forecast error discussed above, the $bias_{NEE}$ of (1) model error (reference model minus observation) distribution of the VPRM model error is asymmetric, as shown in Figure 7. The model bias shows a negative correlation, which means a weaker uptake during the growing season and a weaker respiration during the non-growing season. Data with negative normalized NEE also correspond to a larger bias, which refers to larger model uncertainty during the growing season. The MAE of the model error is 0.166.

3.1.4 Errors at each flux observation site

The MAE is also calculated at each flux measurement site and clustered according to vegetation types, shown in figure 8. Generally the VPRM model error (grey) is larger or similar to the forecast error (blue), consistent with Table 3. Moreover the forecast error does not differ significantly over different vegetation types. Figure 9 shows the error contribution from each source, the meteorological error (error (2) in dark blue and error (3) in light blue) at each site is also the dominant contributor, and has a similar contribution for different vegetation types. The data truncation error (4) has a stronger influence on some grass sites, because EVI at these sites is highly variable, possibly due to mowing and re-growing during the growing season. Overall, except the data truncation error, all forecast error sources have a similar impact on each flux observation site. This shows that the forecast ability does not vary over different vegetation types.

3.2 Spatial pattern of forecast error

The forecast errors are also tested on the European domain from March to June (the season over which the CoMet campaign took place) in 2014, to analyze its spatial patterns. Three experiments have been done to represent the meteorological error (includes analysis error and met forecast error), the MODIS error (including extrapolation error and data truncation error) and the total forecast error (a combination of meteorological error and MODIS error). Figure 10 shows the mean VPRM NEE during the period and the corresponding spatial distribution of each error (in MAE).

https://doi.org/10.5194/gmd-2019-173
Preprint. Discussion started: 23 July 2019

Geoscientific Model Development Discussions

By comparing Figures 10(a) and 10(b), it can be seen that the MAE of the total forecast error has a strong spatial relationship with the mean NEE, which indicates that the forecast error has a similar impact in all places. On a spatial level, the meteorological component still dominates compared to the MODIS error.

In the context of atmospheric CO_2 forecasting, the forecast CO_2 concentrations that are influenced by fluxes from larger MAE areas (northern France, Germany and the Balkans) may have a larger bias due to poorer flux prediction in these areas.

The flux budget over the European domain was also calculated and is shown in Figure 11. The carbon budget of the flux forecast model (in dark blue) is close to the original VPRM model (in grey), thus we are able to confidently use this flux forecast model in the atmospheric GHG concentration forecasting system and predict reasonable CO_2 concentrations on synoptic time scales.

As mentioned in the introduction, we are aiming for not only a flux forecast, but finally an atmospheric GHG concentration forecasting system. While this study has quantified how each error source affects the predicted biospheric fluxes, the next step is to use such flux prediction in an atmospheric transport model run in forecast mode, and to assess the prediction error from each source in concentration space.

4 Conclusions

Based on the VPRM model, we developed a forecasting model that can predict biospheric NEE for the next five days, and assess the error contribution from each aspect of forecasting. This CO_2 flux forecast model is a crucial component in an atmospheric CO_2 forecasting system, in which hourly to day-to-day CO_2 flux variability plays an important role. The forecast model inputs are MODIS near-real-time EVI and LSWI, as well as shortwave radiation and temperature from a meteorological forecast model. The error attribution shows that the dominant error is related to the meteorological data, due to poor prediction of clouds and thus an overestimation of shortwave radiation in the meteorological model. Error from MODIS inputs are less important, and using a persistence assumption to predict MODIS indices resulted in smaller errors than a linear extrapolation. Overall the forecasting system error has a MAE of 0.071, which makes the model capable of forecasting CO_2 fluxes on the target time scale. The error contribution is insensitive to vegetation type and consistent over the whole EU domain. The error of the forecasting system is less than the VPRM model error, which means that the system performs sufficiently well for its predictive task. From the spatial distribution of the error, the absolute flux errors are larger in northern France, Germany and the Balkans, which will lead to larger bias in atmospheric CO_2 forecasting system. The assessment of these (and other) errors in concentration space, using measurements from the CoMet mission as reference data, is foreseen as a follow-up study.

Code and data availability. The code for forecast VPRM model and the model outputs are available from http://dx.doi.org/10.17617/3.2d. The code used for model assessment and figure plotting in this paper is also included in the same repository. The flux measurement data can be acquired from FLUXNET2015 database (see DOI in table 1). The MODIS indices data can be acquired from NASA's Earth Science Data Systems (https://earthdata.nasa.gov/). The ECMWF meteorology data can be retrieved using ECMWF's Meteorological Archival and Retrieval System (MARS, https://confluence.ecmwf.int/display/UDOC/MARS+user+documentation).

Author contribution. The experiments were planned by C. Gerbig, J. Marshall, K.U. Totsche and J. Chen. C. Gerbig prepared the standard VPRM model. J. Chen made the forecast model and performed the model simulation and assessment. J. Marshall extensively commented and revised the manuscript. J. Chen prepared the manuscript with contribution from all co-authors.

Acknowledgements. We acknowledge funding for the CoMet campaign by MPG (Max Planck society) and by BMBF (German Federal Ministry of Education and Research) through AIRSPACE (FK 01LK1701C), and the PhD project funding from the International Max Planck Research School for Global Biogeochemical Cycles (IMPRS-gBGC). We acknowledge the use of data products from the Land, Atmosphere Near real-time Capability for EOS (LANCE) system operated by NASA's Earth Science Data and Information System (ESDIS) with funding provided by NASA Headquarters. We acknowledge ECMWF for providing access to the ECMWF's archived data. This work used eddy covariance data acquired and shared by the FLUXNET community, including these networks: AmeriFlux, AfriFlux, AsiaFlux, CarboAfrica, CarboEuropeIP, CarboItaly, CarboMont, ChinaFlux, Fluxnet-Canada, GreenGrass, ICOS, KoFlux, LBA, NECC, OzFlux-TERN, TCOS-Siberia, and USCCC. The ERA-Interim reanalysis data are provided by ECMWF and processed by LSCE. The FLUXNET eddy covariance data processing and harmonization was carried out by the European Fluxes Database Cluster, AmeriFlux Management Project, and Fluxdata project of FLUXNET, with the support of CDIAC and ICOS Ecosystem Thematic Center, and the OzFlux, ChinaFlux and AsiaFlux offices.

References

Agusti-Panareda, A., Massart, S., Chevallier, F., Boussetta, S., Balsamo, G., Beljaars, A., Ciais, P., Deutscher, N. M., Engelen, R., Jones, L., Kivi, R., Paris, J. D., Peuch, V. H., Sherlock, V., Vermeulen, A. T., Wennberg, P. O., and Wunch, D.: Forecasting global atmospheric CO2, Atmos Chem Phys, 14, 11959-11983, 10.5194/acp-14-11959-2014, 2014.

Agusti-Panareda, A., Massart, S., Chevallier, F., Balsamo, G., Boussetta, S., Dutra, E., and Beljaars, A.: A biogenic CO2 flux adjustment scheme for the mitigation of large-scale biases in global atmospheric CO2 analyses and forecasts, Atmos Chem Phys, 16, 10399-10418, 10.5194/acp-16-10399-2016, 2016.

Amediek, A., Ehret, G., Fix, A., Wirth, M., Budenbender, C., Quatrevalet, M., Kiemle, C., and Gerbig, C.: CHARM-F-a new airborne integrated-path differential-absorption lidar for carbon dioxide and methane observations: measurement performance and quantification of strong point source emissions, Appl Optics, 56, 5182-5197, 10.1364/Ao.56.005182, 2017.

https://doi.org/10.5194/gmd-2019-173
Preprint. Discussion started: 23 July 2019

Geoscientific Model Development Discussions
Open Access

Anthoni, P., Knohl, A., Rebmann, C., Freibauer, A., Mund, M., Ziegler, W., Kolle, O., and Schulze, E. D.: Forest and agricultural land ‐ use ‐ dependent CO_2 exchange in Thuringia, Germany, Global Change Biology, 10, 2005-2019, 2004.

Aubinet, M., Chermanne, B., Vandenhaute, M., Longdoz, B., Yernaux, M., and Laitat, E.: Long term carbon dioxide exchange above a mixed forest in the Belgian Ardennes, Agricultural and Forest Meteorology, 108, 293-315, 2001.

Aulagnier, C., Rayner, P., Ciais, P., Vautard, R., Rivier, L., and Ramonet, M.: Is the recent build-up of atmospheric CO_2 over Europe reproduced by models. Part 2: an overview with the atmospheric mesoscale transport model CHIMERE, Tellus B, 62, 14-25, 10.1111/j.1600-0889.2009.00443.x, 2010.

Baldocchi, D., Falge, E., Gu, L., Olson, R., Hollinger, D., Running, S., Anthoni, P., Bernhofer, C., Davis, K., and Evans, R.: FLUXNET: A new tool to study the temporal and spatial variability of ecosystem-scale carbon dioxide, water vapor, and energy flux densities, Bulletin of the American Meteorological Society, 82, 2415-2434, 2001.

Beck, V., Koch, T., Kretschmer, R., Marshall, J., Ahmadov, R., Gerbig, C., Pillai, D., and Heimann, M.: The WRF Greenhouse Gas Model (WRF-GHG), Technical Report No. 25, Max Planck Institute for Biogeochemistry, Jena, Germany, available at: http://www.bgc-jena.mpg.de/bgc-systems/index.shtml 2011.

Bernhofer, C., Grünwald, T., Moderow, U., Hehn, M., Eichelmann, U., and Prasse, H.: FLUXNET2015 DE-Spw Spreewald, 10.18140/FLX/1440220,

Boussetta, S., Balsamo, G., Beljaars, A., Panareda, A. A., Calvet, J. C., Jacobs, C., van den Hurk, B., Viterbo, P., Lafont, S., Dutra, E., Jarlan, L., Balzarolo, M., Papale, D., and van der Werf, G.: Natural land carbon dioxide exchanges in the ECMWF integrated forecasting system: Implementation and offline validation, J Geophys Res-Atmos, 118, 5923-5946, 10.1002/jgrd.50488, 2013.

Butz, A., Dinger, A. S., Bobrowski, N., Kostinek, J., Fieber, L., Fischerkeller, C., Giuffrida, G. B., Hase, F., Klappenbach, F., and Kuhn, J.: Remote sensing of volcanic CO_2, HF, HCl, SO_2, and BrO in the downwind plume of Mt. Etna, Atmos Meas Tech, 2017.

Delpierre, N., Berveiller, D., Granda, E., and Dufrêne, E.: Wood phenology, not carbon input, controls the interannual variability of wood growth in a temperate oak forest, New Phytologist, 210, 459-470, 2016.

Dietiker, D., Buchmann, N., and Eugster, W.: Testing the ability of the DNDC model to predict CO_2 and water vapour fluxes of a Swiss cropland site, Agriculture, ecosystems & environment, 139, 396-401, 2010.

Dušek, J., Čížková, H., Stellner, S., Czerný, R., and Květ, J.: Fluctuating water table affects gross ecosystem production and gross radiation use efficiency in a sedge-grass marsh, Hydrobiologia, 692, 57-66, 2012.

Etzold, S., Ruehr, N. K., Zweifel, R., Dobbertin, M., Zingg, A., Pluess, P., Häsler, R., Eugster, W., and Buchmann, N.: The carbon balance of two contrasting mountain forest ecosystems in Switzerland: similar annual trends, but seasonal differences, Ecosystems, 14, 1289-1309, 2011.

https://doi.org/10.5194/gmd-2019-173
Preprint. Discussion started: 23 July 2019

Fares, S., Savi, F., Muller, J., Matteucci, G., and Paoletti, E.: Simultaneous measurements of above and below canopy ozone fluxes help partitioning ozone deposition between its various sinks in a Mediterranean Oak Forest, Agricultural and forest meteorology, 198, 181-191, 2014.

Ferréa, C., Zenone, T., Comolli, R., and Seufert, G.: Estimating heterotrophic and autotrophic soil respiration in a semi-natural forest of Lombardy, Italy, Pedobiologia, 55, 285-294, 2012.

Galvagno, M., Wohlfahrt, G., Cremonese, E., Rossini, M., Colombo, R., Filippa, G., Julitta, T., Manca, G., Siniscalco, C., and di Cella, U. M.: Phenology and carbon dioxide source/sink strength of a subalpine grassland in response to an exceptionally short snow season, Environmental Research Letters, 8, 025008, 2013.

Gerilowski, K., Tretner, A., Krings, T., Buchwitz, M., Bertagnolio, P. P., Belemezov, F., Erzinger, J., Burrows, J. P., and Bovensmann, H.: MAMAP - a new spectrometer system for column-averaged methane and carbon dioxide observations from aircraft: instrument description and performance analysis, Atmos Meas Tech, 4, 215-243, 10.5194/amt-4-215-2011, 2011.

GrüNwald, T., and Bernhofer, C.: A decade of carbon, water and energy flux measurements of an old spruce forest at the Anchor Station Tharandt, Tellus B: Chemical and Physical Meteorology, 59, 387-396, 2007.

Hommeltenberg, J., Schmid, H., Drösler, M., and Werle, P.: Can a bog drained for forestry be a stronger carbon sink than a natural bog forest?, Biogeosciences, 11, 3477-3493, 2014.

Imer, D., Merbold, L., Eugster, W., and Buchmann, N.: Temporal and spatial variations of soil CO 2, CH 4 and N 2 O fluxes at three differently managed grasslands, Biogeosciences, 10, 5931-5945, 2013.

IPCC: Climate Change 2014: Synthesis Report. Contribution of Working Groups I, II, and III to the Fifth Assessment Report of the Intergovernmental Panel on Climate Change [Core Writing Team, R.K. Pachauri and L.A. Meyer (eds.)], IPCC, Geneva, Switzerland, 151 pp., 2014.

Jung, M., Henkel, K., Herold, M., and Churkina, G.: Exploiting synergies of global land cover products for carbon cycle modeling, Remote Sens Environ, 101, 534-553, 2006.

Kountouris, P., Gerbig, C., Rödenbeck, C., Karstens, U., Koch, T. F., and Heimann, M.: Atmospheric CO 2 inversions on the mesoscale using data-driven prior uncertainties: methodology and system evaluation, Atmos Chem Phys, 18, 3027-3045, 2018.

Le Quere, C., Raupach, M. R., Canadell, J. G., Marland, G., Bopp, L., Ciais, P., Conway, T. J., Doney, S. C., Feely, R. A., Foster, P., Friedlingstein, P., Gurney, K., Houghton, R. A., House, J. I., Huntingford, C., Levy, P. E., Lomas, M. R., Majkut, J., Metzl, N., Ometto, J. P., Peters, G. P., Prentice, I. C., Randerson, J. T., Running, S. W., Sarmiento, J. L., Schuster, U., Sitch, S., Takahashi, T., Viovy, N., van der Werf, G. R., and Woodward, F. I.: Trends in the sources and sinks of carbon dioxide, Nat Geosci, 2, 831-836, 10.1038/ngeo689, 2009.

Lin, J. C., Pejam, M. R., Chan, E., Wofsy, S. C., Gottlieb, E. W., Margolis, H. A., and McCaughey, J. H.: Attributing uncertainties in simulated biospheric carbon fluxes to different error sources, Global Biogeochem Cy, 25, Artn Gb2018
10.1029/2010gb003884, 2011.

Mahadevan, P., Wofsy, S. C., Matross, D. M., Xiao, X. M., Dunn, A. L., Lin, J. C., Gerbig, C., Munger, J. W., Chow, V. Y., and Gottlieb, E. W.: A satellite-based biosphere parameterization for net

https://doi.org/10.5194/gmd-2019-173
Preprint. Discussion started: 23 July 2019

ecosystem CO_2 exchange: Vegetation Photosynthesis and Respiration Model (VPRM), Global Biogeochem Cy, 22, Artn Gb2005 10.1029/2006gb002735, 2008.

Marcolla, B., Pitacco, A., and Cescatti, A.: Canopy architecture and turbulence structure in a coniferous forest, Boundary-layer meteorology, 108, 39-59, 2003.

Mauder, M., Cuntz, M., Drüe, C., Graf, A., Rebmann, C., Schmid, H. P., Schmidt, M., and Steinbrecher, R.: A strategy for quality and uncertainty assessment of long-term eddy-covariance measurements, Agricultural and Forest Meteorology, 169, 122-135, 2013.

Merbold, L., Eugster, W., Stieger, J., Zahniser, M., Nelson, D., and Buchmann, N.: Greenhouse gas budget (CO_2, CH_4 and N_2O) of intensively managed grassland following restoration, Global change biology, 20, 1913-1928, 2014.

Moureaux, C., Debacq, A., Bodson, B., Heinesch, B., and Aubinet, M.: Annual net ecosystem carbon exchange by a sugar beet crop, Agricultural and Forest Meteorology, 139, 25-39, 2006.

Pilegaard, K., Ibrom, A., Courtney, M. S., Hummelshøj, P., and Jensen, N. O.: Increasing net CO_2 uptake by a Danish beech forest during the period from 1996 to 2009, Agricultural and Forest Meteorology, 151, 934-946, 2011.

Pillai, D., Buchwitz, M., Gerbig, C., Koch, T., Reuter, M., Bovensmann, H., Marshall, J., and Burrows, J. P.: Tracking city CO_2 emissions from space using a high-resolution inverse modelling approach: a case study for Berlin, Germany, Atmos Chem Phys, 16, 9591-9610, 10.5194/acp-16-9591-2016, 2016.

Post, H., Hendricks Franssen, H.-J., Graf, A., Schmidt, M., and Vereecken, H.: Uncertainty analysis of eddy covariance CO_2 flux measurements for different EC tower distances using an extended two-tower approach, Biogeosciences, 12, 1205-1221, 2015.

Potter, C. S., Randerson, J. T., Field, C. B., Matson, P. A., Vitousek, P. M., Mooney, H. A., and Klooster, S. A.: Terrestrial Ecosystem Production - a Process Model-Based on Global Satellite and Surface Data, Global Biogeochem Cy, 7, 811-841, Doi 10.1029/93gb02725, 1993.

Prescher, A.-K., Grünwald, T., and Bernhofer, C.: Land use regulates carbon budgets in eastern Germany: From NEE to NBP, Agricultural and Forest Meteorology, 150, 1016-1025, 2010.

Rambal, S., Joffre, R., Ourcival, J., Cavender‐Bares, J., and Rocheteau, A.: The growth respiration component in eddy CO_2 flux from a Quercus ilex mediterranean forest, Global Change Biology, 10, 1460-1469, 2004.

Running, S. W., and Hunt Jr, E. R.: Generalization of a forest ecosystem process model for other biomes, BIOME-BCG, and an application for global-scale models, 1993.

Running, S. W., Thornton, P. E., Nemani, R., and Glassy, J. M.: Global terrestrial gross and net primary productivity from the Earth Observing System, in: Methods in ecosystem science, Springer, 44-57, 2000.

Sabbatini, S., Arriga, N., Bertolini, T., Castaldi, S., Chiti, T., Consalvo, C., Djomo, S. N., Gioli, B., Matteucci, G., and Papale, D.: Greenhouse gas balance of cropland conversion to bioenergy poplar short-rotation coppice, Biogeosciences, 13, 95-113, 2016.

https://doi.org/10.5194/gmd-2019-173
Preprint. Discussion started: 23 July 2019

Suni, T., Rinne, J., Reissell, A., Altimir, N., Keronen, P., Rannik, U., Maso, M., Kulmala, M., and Vesala, T.: Long-term measurements of surface fluxes above a Scots pine forest in Hyytiala, southern Finland, 1996-2001, Boreal Environment Research, 8, 287-302, 2003.

Thum, T., Aalto, T., Laurila, T., Aurela, M., Kolari, P., and Hari, P.: Parametrization of two photosynthesis models at the canopy scale in a northern boreal Scots pine forest, Tellus B, 59, 874-890, 2007.

Valentini, R., De Angelis, P., Matteucci, G., Monaco, R., Dore, S., and Mucnozza, G. S.: Seasonal net carbon dioxide exchange of a beech forest with the atmosphere, Global Change Biology, 2, 199-207, 1996.

Vitale, L., Di Tommasi, P., D'Urso, G., and Magliulo, V.: The response of ecosystem carbon fluxes to LAI and environmental drivers in a maize crop grown in two contrasting seasons, International journal of biometeorology, 60, 411-420, 2016.

Woodward, F. I., Smith, T. M., and Emanuel, W. R.: A Global Land Primary Productivity and Phytogeography Model, Global Biogeochem Cy, 9, 471-490, Doi 10.1029/95gb02432, 1995.

Xiao, X. M., Hollinger, D., Aber, J., Goltz, M., Davidson, E. A., Zhang, Q. Y., and Moore, B.: Satellite-based modeling of gross primary production in an evergreen needleleaf forest, Remote Sens Environ, 89, 519-534, 10.1016/j.rse.2003.11.008, 2004.

Zhuang, Q., McGuire, A. D., Melillo, J. M., Clein, J. S., Dargaville, R. J., Kicklighter, D. W., Myneni, R. B., Dong, J., Romanovsky, V. E., Harden, J., and Hobbie, J. E.: Carbon cycling in extratropical terrestrial ecosystems of the Northern Hemisphere during the 20th century: a modeling analysis of the influences of soil thermal dynamics, Tellus B, 55, 751-776, DOI 10.1034/j.1600-0889.2003.00060.x, 2003.

Zielis, S., Etzold, S., Zweifel, R., Eugster, W., Haeni, M., and Buchmann, N.: NEP of a Swiss subalpine forest is significantly driven not only by current but also by previous year's weather, Biogeosciences, 11, 1627-1635, 2014.

https://doi.org/10.5194/gmd-2019-173
Preprint. Discussion started: 23 July 2019

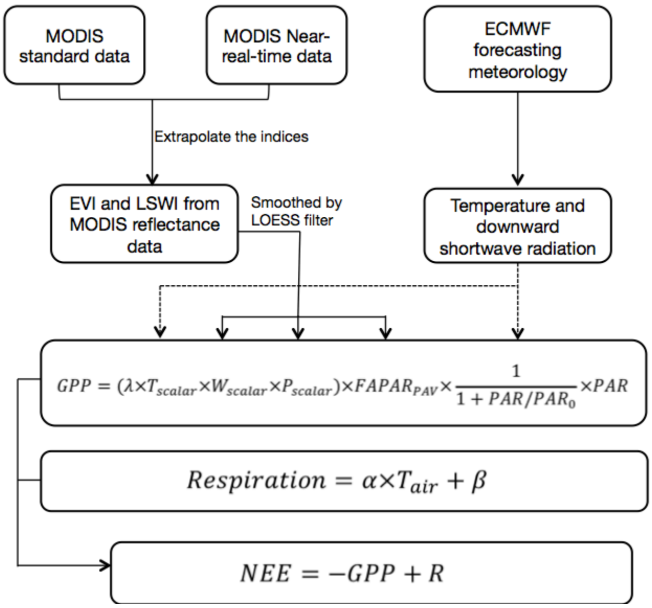

Figure 1: Diagram of the VPRM forecasting system. The top two levels show the drivers which are predicted into the future, while the bottom three boxes are based on the standard VPRM model (Mahadevan et al., 2008).

https://doi.org/10.5194/gmd-2019-173
Preprint. Discussion started: 23 July 2019

Site ID	Latitude	Longitude	Vegetation types in VPRM	Data DOI	Reference
BE-Bra	51,3092	4,5206	Mixfrst	10.18140/FLX/1440128	(Janssens et al.)
BE-Lon	50,5516	4,7461	Crop	10.18140/FLX/1440129	(Moureaux et al., 2006)
BE-Vie	50,3051	5,9981	Mixfrst	10.18140/FLX/1440130	(Aubinet et al., 2001)
CH-Cha	47,2102	8,4104	Grass	10.18140/FLX/1440131	(Merbold et al., 2014)
CH-Dav	46,8153	9,8559	Evergreen	10.18140/FLX/1440132	(Zielis et al., 2014)
CH-Fru	47,1158	8,5378	Grass	10.18140/FLX/1440133	(Imer et al., 2013)
CH-Lae	47,4781	8,365	Mixfrst	10.18140/FLX/1440134	(Etzold et al., 2011)
CH-Oe2	47,2863	7,7343	Crop	10.18140/FLX/1440136	(Dietiker et al., 2010)
CZ-wet	49,0247	14,7704	Grass	10.18140/FLX/1440145	(Dušek et al., 2012)
DE-Akm	53,8662	13,6834	Grass	10.18140/FLX/1440213	(Bernhofer et al.)
DE-Geb	51,1001	10,9143	Crop	10.18140/FLX/1440146	(Anthoni et al., 2004)
DE-Gri	50,9495	13,5125	Grass	10.18140/FLX/1440147	(Prescher et al., 2010)
DE-Kli	50,8929	13,5225	Crop	10.18140/FLX/1440149	(Prescher et al., 2010)
DE-Obe	50,7836	13,7196	Evergreen	10.18140/FLX/1440151	(Bernhofer et al.)
DE-RuR	50,6219	6,3041	Grass	10.18140/FLX/1440215	(Post et al., 2015)
DE-RuS	50,8659	6,4472	Crop	10.18140/FLX/1440216	(Mauder et al., 2013)
DE-SfN	47,8064	11,3275	Grass	10.18140/FLX/1440219	(Hommeltenberg et al., 2014)
DE-Spw	51,8923	14,0337	Grass	10.18140/FLX/1440220	(Bernhofer et al.)
DE-Tha	50,9636	13,5669	Evergreen	10.18140/FLX/1440152	(GrüNwald and Bernhofer, 2007)
DK-Sor	55,4859	11,6446	Decid	10.18140/FLX/1440155	(Pilegaard et al., 2011)
FI-Hyy	61,8475	24,295	Evergreen	10.18140/FLX/1440158	(Suni et al., 2003)
FI-Sod	67,3619	26,6378	Evergreen	10.18140/FLX/1440160	(Thum et al., 2007)
FR-Fon	48,4764	2,7801	Decid	10.18140/FLX/1440161	(Delpierre et al., 2016)
FR-Pue	43,7414	3,5958	Evergreen	10.18140/FLX/1440164	(Rambal et al., 2004)
IT-BCi	40,5238	14,9574	Crop	10.18140/FLX/1440166	(Vitale et al., 2016)
IT-CA1	42,3804	12,0266	Decid	10.18140/FLX/1440230	(Sabbatini et al., 2016)
IT-CA2	42,3772	12,026	Crop	10.18140/FLX/1440231	(Sabbatini et al., 2016)
IT-CA3	42,38	12,0222	Decid	10.18140/FLX/1440232	(Sabbatini et al., 2016)
IT-Col	41,8494	13,5881	Decid	10.18140/FLX/1440167	(Valentini et al., 1996)
IT-Cp2	41,7043	12,3573	Evergreen	10.18140/FLX/1440233	(Fares et al., 2014)
IT-Isp	45,8126	8,6336	Decid	10.18140/FLX/1440234	(Ferréa et al., 2012)
IT-Lav	45,9562	11,2813	Evergreen	10.18140/FLX/1440169	(Marcolla et al., 2003)
IT-Tor	45,8444	7,5781	Grass	10.18140/FLX/1440237	(Galvagno et al., 2013)

Table 1: The selected FLUXNET2015 sites used for data-model comparison in this research.

590

https://doi.org/10.5194/gmd-2019-173
Preprint. Discussion started: 23 July 2019

Geoscientific Model Development
Discussions
Open Access
EGU

	MODIS indices	Meteorology data	Error sources
Reference simulation	Standard MODIS products	Flux site observation	(1)
Simulation a	Standard MODIS products	ECMWF 12h forecasting	(1)+(2)
Simulation b	Standard MODIS products	ECMWF 5th day forecasting	(1)+(2)+(3)
Simulation c	Truncated MODIS indices	Flux site observation	(1)+(5)
Simulation d	MODIS prediction based on fully filtered data	Flux site observation	(1)+(6)
Simulation e	NRT MODIS indices	Flux site observation	(1)+(4)
Simulation f	MODIS prediction based on truncated data	ECMWF 5th day forecasting	(1)+(2)+(3)+(5)+(6)

Table 2: The experiment setup and the error sources addressed in each simulation. The numbering in the last column corresponds to the error from (1) the VPRM model, (2) the meteorological analysis, (3) the meteorological forecast, (4) the MODIS NRT data, (5) data truncation and (6) the prediction of MODIS indices.

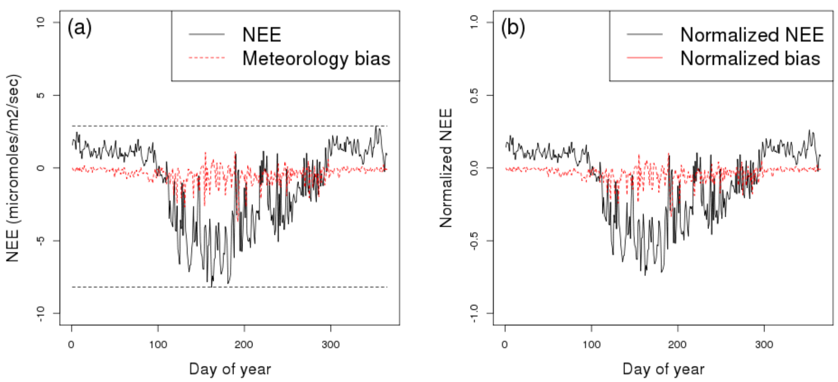

Figure 2: Example of the data normalization at station BE-Bra: (a) NEE output from simulation a, and the corresponding biasNEE. The dashed black lines show the range of annual NEE. (b) NEE and bias after normalization by the range, conserving the physical meaning (release and uptake) of the sign.

https://doi.org/10.5194/gmd-2019-173
Preprint. Discussion started: 23 July 2019

Normalized Mean Absolute Error (MAE) for each error source		
Compared objects	**Error sources**	**MAE**
a-ref.	(2) Meteorological analysis	0.046
b-a	(3) Meteorological forecast	0.040
b-ref.	(2)+(3) Meteorological error	0.065
c-ref.	(5) Data truncation	0.015
d-ref.	(6a-i) Linear EVI	0.016
d-ref.	(6a-ii) Persistence EVI	0.013
d-ref.	(6b-i) Linear LSWI	0.012
d-ref.	(6b-ii) Persistence LSWI	0.010
f-ref.	(2)+(3)+(5)+(6a-ii)+(6b-ii) Forecast error	0.071
ref.-obs.	(1) Model error	0.159

Table 3: Normalized Mean Absolute error (MAE) for each error source. The compared objects are simulation a to f, the reference simulation (ref.) and FLUXNET observation (obs.). Error sources (1) to (6) described in 2.2 can be isolated by calculating the MAE between different simulations.

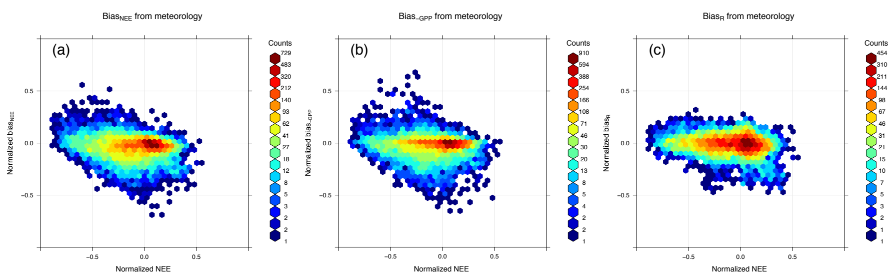

Figure 3: (a) Distribution of normalized biasNEE due to meteorological error. The x-axis refers to the normalized NEE, and the y-axis refers to the corresponding biasNEE defined in section 2.2. Panels (b) and (c) share the same x-axis with (a), but have bias-GPP and biasR in y-axis instead. The three biases combine as biasNEE= bias-GPP + biasR, indicating that biasNEE is dominated by bias-GPP, which is controlled by the radiation parameter rather than temperature.

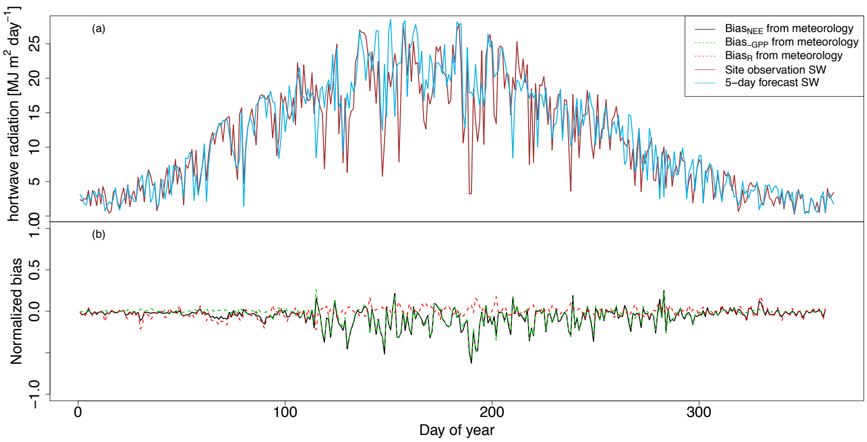

625 **Figure 4: (a) Downward shortwave radiation from site-level measurement and from 5-day forecasts at station BE-Bra. (b) biasNEE, bias-GPP and biasR at station BE-Bra. As the biases are combined as biasNEE= bias-GPP + biasR, this figure confirms that the large negative biasNEE is due to bias-GPP, and the reason is that NWP overestimate SW for cloudy days in summer.**

https://doi.org/10.5194/gmd-2019-173
Preprint. Discussion started: 23 July 2019

Geoscientific Model Development
Discussions
Open Access
EGU

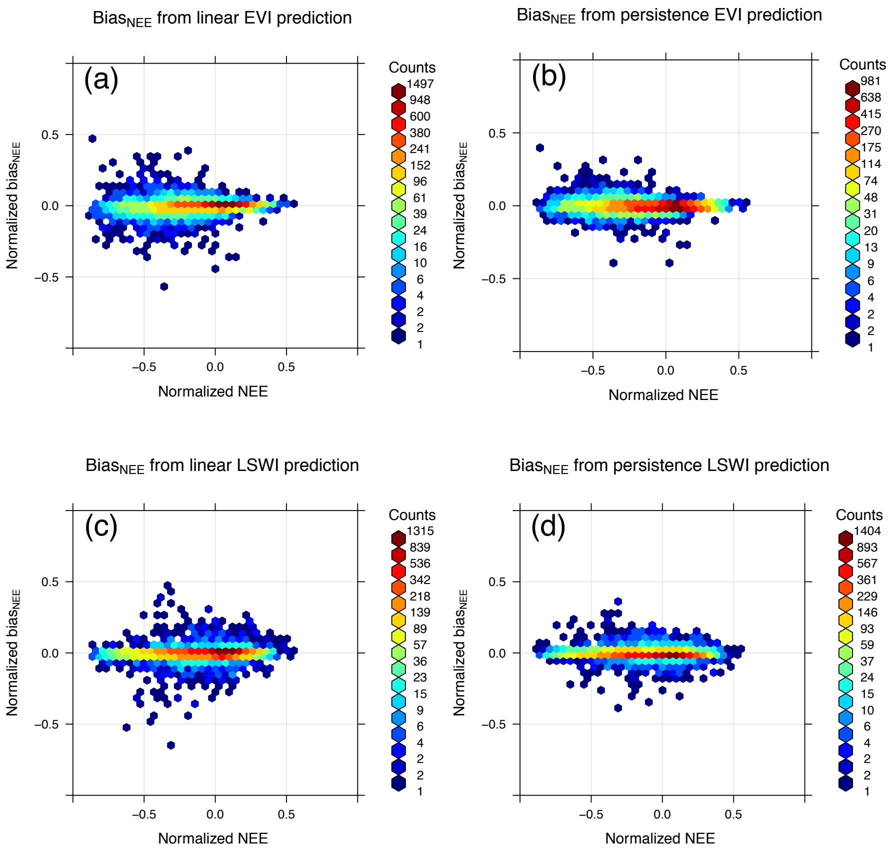

Figure 5: biasNEE distribution of using linear extrapolation or persistence to predict EVI and LSWI. The persistence prediction introduces less bias than linear extrapolation for both EVI and LSWI. Therefore persistence is used in the final forecast.

NEE sensitivity to EVI			NEE sensitivity to LSWI		
Seasons	Sensitivity [μmole m^{-2} s^{-1} EVI^{-1}]	R^2	Seasons	Sensitivity [μmole m^{-2} s^{-1} LSWI^{-1}]	R^2
Dec - Feb	-0.90	0.27	Dec - Feb	-0.57	0.28
Mar - May	-7.96	0.64	Mar - May	-3.41	0.51
Jun - Aug	-9.11	0.74	Jun - Aug	-6.29	0.58
Sep - Jan	-2.70	0.35	Sep - Jan	-1.16	0.29

Table 4: The model's sensitivity of NEE to EVI/LSWI for four seasons. The result of simulation d is used in the sensitivity calculation. Linear regression is applied to the change in EVI and the change in corresponding NEE, the maximum sensitivity appears in summer, with a slope of -10.73 [μmole m-2 s-1 EVI-1] for EVI and -6.29 [μmole m-2 s-1 LSWI-1] for LSWI respectively.

https://doi.org/10.5194/gmd-2019-173
Preprint. Discussion started: 23 July 2019

Geoscientific Model Development
Discussions

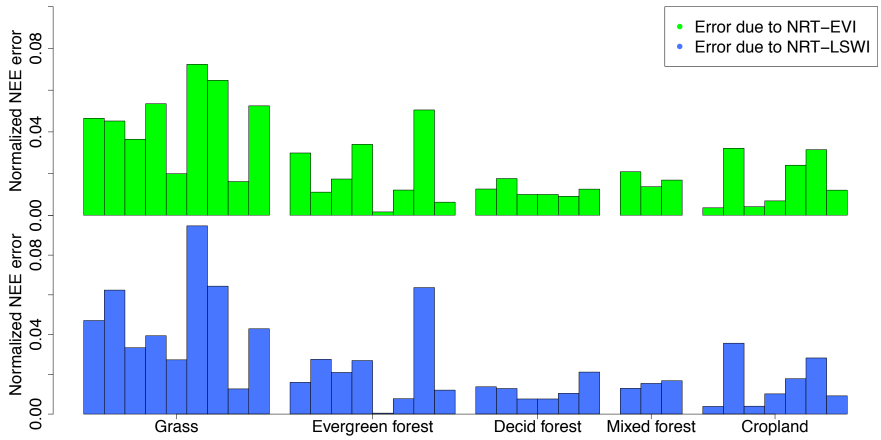

640

Figure 6: The normalized error of NEE as a result of MODIS NRT error at 33 sites. 120 days from February to June in the year 2018 of MODIS NRT data are used to first calculate the EVI/LSWI differences, then times the sensitivities in table 4 and normalized by the same scalar in the previous research. The flux sites in x-axis are sorted by vegetation type and FLUXNET site-ID (from left to right:
645 **CH-Cha, CH-Fru, CZ-wet, DE-Akm, DE-Gri, DE-RuR, DE-SfN, DE-Spw, IT-Tor, CH-Dav, DE-Obe, DE-Tha, FI-Hyy, FI-Sod, FR-Pue, IT-Cp2, IT-Lav, DK-Sor, FR-Fon, IT-CA1, IT-CA3, IT-Col, IT-Isp, BE-Bra, BE-Vie, CH-Lae, BE-Lon, CH-Oe2, DE-Geb, DE-Kli, DE-Rus, IT-BCi, IT-CA2).**

https://doi.org/10.5194/gmd-2019-173
Preprint. Discussion started: 23 July 2019

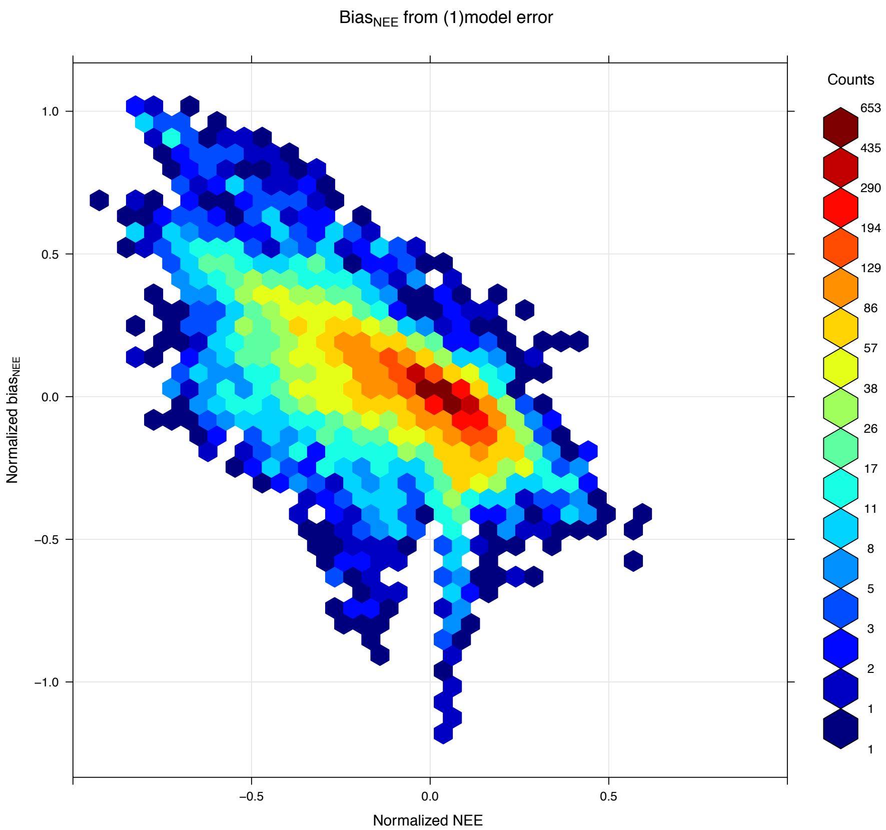

Figure 7: The biasNEE distribution of the VPRM model error.

650

https://doi.org/10.5194/gmd-2019-173
Preprint. Discussion started: 23 July 2019

Geoscientific Model Development
Open Access
Discussions

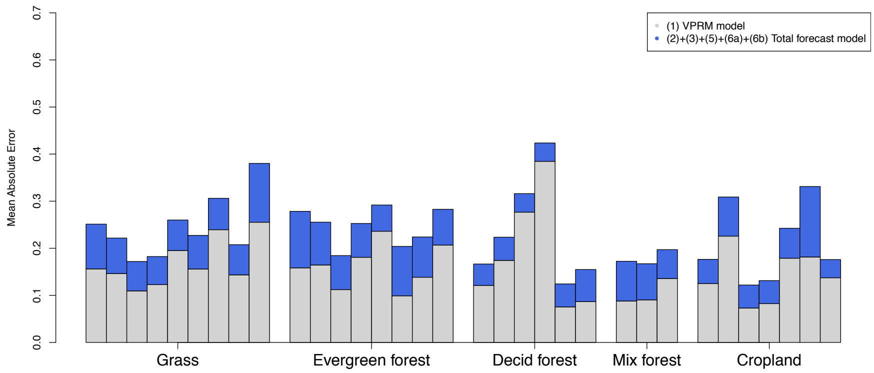

655 **Figure 8: Mean absolute error of the forecast error compared to the VPRM model error at each flux observation site. The model error (1) is generally larger than the total forecast error (2) to (6), and the forecast error does not differ significantly across vegetation types. The order of the flux site is the same as in figure 6.**

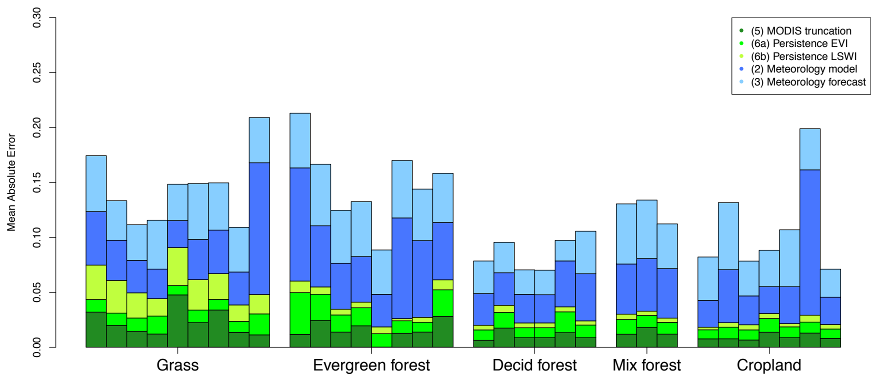

660 **Figure 9: Mean absolute error for different error sources at each flux observation site. The meteorological error ((2)meteorological model + (3)meteorological forecast) is the dominant contributor at each site, and has a similar contribution for different vegetation types. The data truncation error (4) has a stronger influence on some grass sites, likely due to the highly EVI variability resulting from mowing and regrowth during the growing season. The order of the flux site is the same as in figure 6.**

https://doi.org/10.5194/gmd-2019-173
Preprint. Discussion started: 23 July 2019

Geoscientific Model Development
Discussions

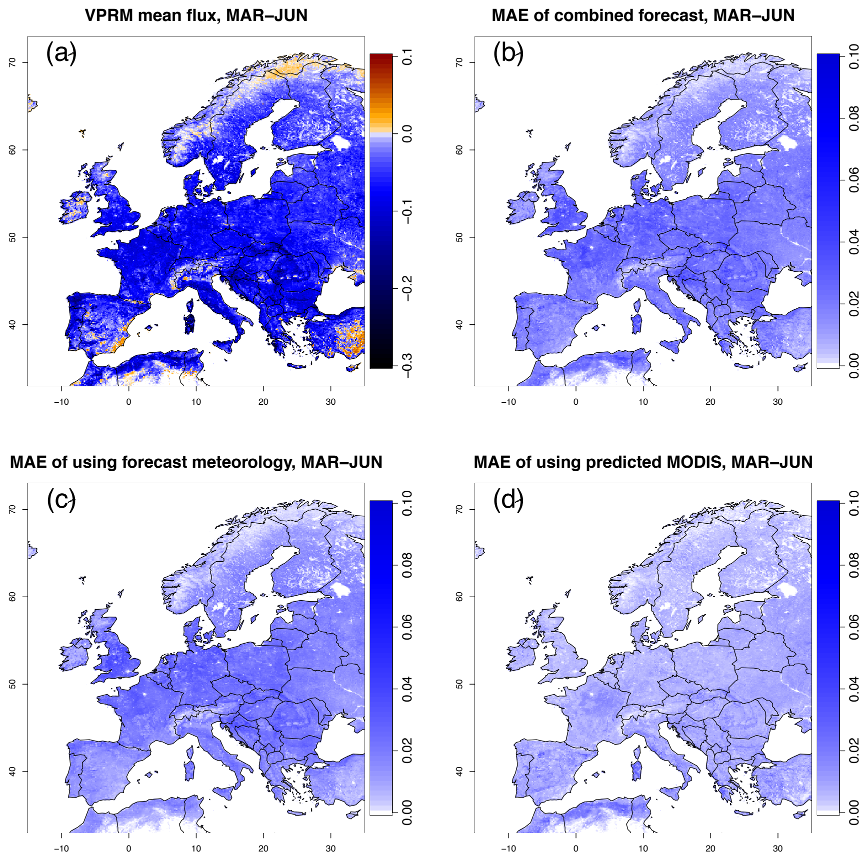

665 **Figure 10: (a) Mean VPRM NEE, during March to June 2014; (b) Spatial distribution of MAE for forecast error; (c) spatial distribution of MAE for meteorological error; (d) spatial distribution of MAE for MODIS error. The MAE of total forecast error in (b) has strong spatial relationship with the VPRM mean flux in (a), which indicates that the forecast error has a similar impact in all places. Panels (c) and (d) are consistent with table 3, in that the forecast error is larger than the error from MODIS prediction.**

https://doi.org/10.5194/gmd-2019-173
Preprint. Discussion started: 23 July 2019

Geoscientific Model Development
Discussions
Open Access
EGU

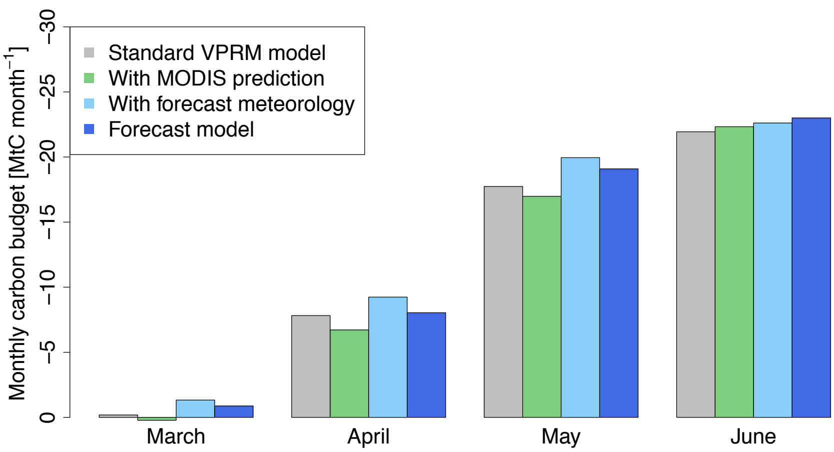

Figure 11: Monthly carbon budget from March to June for original and forecast model for the European domain. The overall forecast flux budget is close to the original model, indicating the forecast flux model is appropriate for use in the GHG concentration forecasting system.

675